McGill University

ECSE527

Final Report

High-Speed Line-Scan Spectral-Domain Optical Coherence Tomography System for Retinal Cell Deformation Detection in Human Eye

Team Member 1:	Hossen Alyazgi (261313569)
Team Member 2:	Hayden Snauwaert (261311511)
Instructor:	Dr. Andrew Kirk
Date:	April 19, 2026

Department of Electrical and Computer Engineering

I. Introduction

VISION in mammals arises from photochemical and biological processes in the eye. In humans, photoreceptors that populate the retina possess varied sensitivities to different wavelengths of light are what enable colour vision [12]. These receptors two further subdivisions; rods, which are sensitive in low light conditions, and cones, which are active in bright light conditions. Rods exist in a far greater proportion than cones [17], and understanding their dynamics is worthwhile as their (mal)function is a key finding in ailements such as diabetic retinopathy and retinitis pigmentosa [7]. In practice, this can be achieved by directly measuring the activation of the rod cells themselves, as demonstrated in a recent paper by Zhou et al., titled "Interferometric imaging of the reversible rhodopsin dynamics in the living rat eye"[21]. Rhodopsin, being the light-sensitive protein principally involved in triggering the signal cascade of photo-detection in rod cells, induces what is termed an early receptor potential (ERP) upon photo-stimulation, which is the primary electro-chemical signature demonstrating photo-reception. This manifests in a nanoscale deformation of the rod cell body. The authors of the aforementioned study made use of the established technique of optoretinography (ORG), which enables the detection of these specific retinal cell contractions through the use of Optical Coherence Tomography (OCT), itself based on principles of interferometry.

In the context of `ECSE527`, the process of constructing an apparatus that enables this technique implicates design challenges highly relevant to the realm of free space optics. The primary goal of this project was thus established to be the design and implementation of the optical system embedded within the ORG methodology. We took the work of Zhou et al. as a point of departure, but diverged in choosing the human eye as the target of measurement, which requires it's own host of design considerations, but which we believed would an interesting extension of the paper. Indeed, ORG in humans is a highly active field of research and encounters its own unique challenges, metrics, and constraints [5, 15, 10, 4, 20].

Surprisingly, however, the structure of the ORG apparatus remains markedly similar across studies. Consider, as a representative example of human ORG, the optical setup of Pandiyan et al. in Fig. 2 in comparison to that of Zhou et al. in Fig. 3. The exact mechanism of obtaining the optoretinogram will be discussed in subsequent sections, but what is important to observe is that there are 6 shared main paths, described in Table. VIII. The only path that is not shared between the two is the wavefront sensing path, which only exists with the design presented by Pandiyan et al. to produce an estimate of ocular aberration and drive the deformable

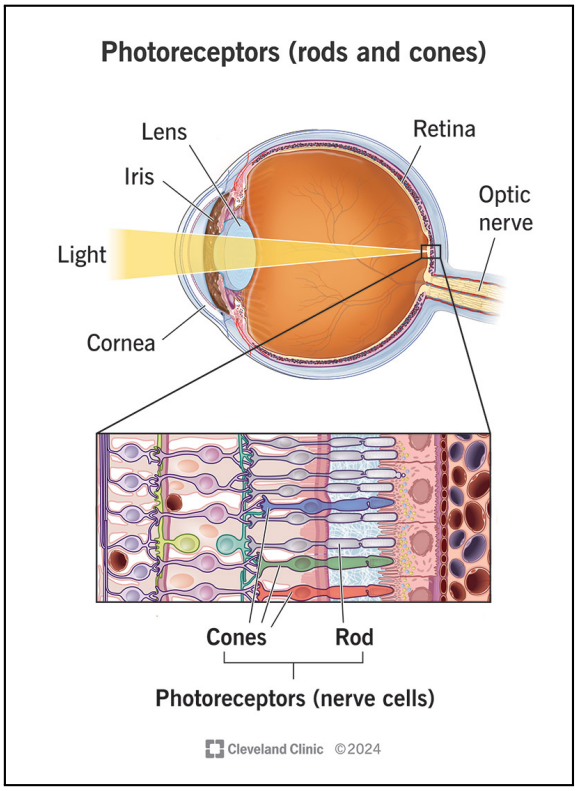

Fig. 1: Location and orientation of rod and cone photoreceptors in the human eye. Excerpted from [18]

mirror. This highlights the subtle differences that arise based on the *intent* of the imaging. Sensitivity to aberrations is only (highly) important when lateral resolution is of concern, i.e. when resolving the cell itself is an objective, a noted weakness of OCT technology in general [20]. On the other hand, detecting rod contraction, which as observed in Fig. 1, are oriented parallel to incident light as it concerns a directly aimed beam, requires depth-wise — here termed *axial* — resolving capabilities.

With that said, to remain within the confines of the course objectives as well as to scope complexity of the project appropriately, we thus decided to focus our efforts towards designing just the OCT illumination arm and spectrometer path (green highlighted columns in Table. VIII) for rod contraction detection, as these are both critical pathways that present a sufficient design challenge and are amenable to simulation and verification in `CODE V` [11]. There are certain aspects of the design that cannot be strictly enforced. for example, *in vivo* applications require high-scan rate to mitigate phase stability issues due to eye and other physiological motion artifacts, such as heartbeat. This is why, for example, line scanning is used, as it combines multiple point scans, increasing the scan rate. With such cases, we choose to adopt the design choice understanding that its validation is outside the

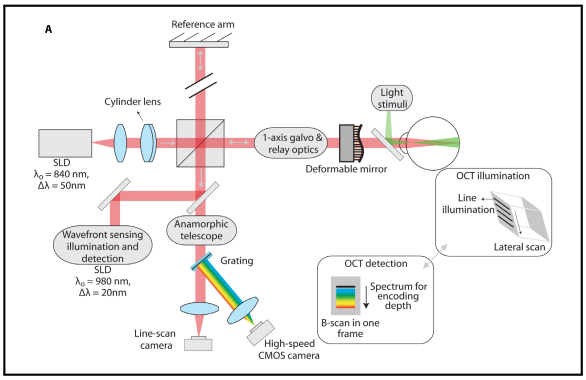

Fig. 2: Optical setup used for OCT imaging and retinal stimulation in human eye. Excerpted from Fig. 5 A of Pandiyan et al. [16].

bounds of optical design per se. As a general rule, we defaulted to adapting from Zhou et al. in terms of material and parameters when it aligned with our aims, and diverged *pro re nata* when it pertains to meeting the conditions of the eye model and design complexity, and attempt to meet clinical conditions of human ORG as outlined by current trends and state of the art[9], we have compiled the following specification outline for the goals of this project in Table. I, with further rationale and derivations of these specifications elaborated upon subsequent sections. Briefly, we justify the choices as follows: Irradiated line length and scan range are both methodological constraints based on prior literature. OCT illumination/BW and lateral resolution are based on the requirement to cellular resolution of rod itself (the contractile region is nominally considered to occupy a volume of 3x3x3 μm [10]). Finally, pupil-conjugation is necessary for mitigating aberrations along scans. These are the foundational constraints that will allow us to meet the project goal of *designing the OCT illumination and detection arms of a human ORG system aimed at rod contractile detection.*

II. Background and Theory

OCT is a non-invasive, interferometric, micrometre-scale imaging technique that enables depth-imaging of weakly scattering samples, such as biological tissues. The technique operates on the principle of low-coherence interferometry, where light from a broadband source is split by a Michelson interferometer between the sample and a reference arm. Under the condition that the recombinant beams have a fixed phase relationship, which is obtainable by ensuring that the optical path length traversed by the sample and reference beams differ only by the source coherence length, interference can be observed [3]. The coherent waves can recombine constructively, destructively, or meet any condition in between to produce an interference signal with a series of bright and dark fringes. Receiving this signal with a detector allows information about the scattering bodies in the sample to be extracted electronically. In SD-OCT, the beam is separated in to its spectral components using a diffraction grating prior to detection, creating a spectral interferogram, where separate frequency components are mapped to one spatial axis on the detector. Information about the depth and reflectivity of the nth scattering element in the sample is encoded by intensity ripples in the spectral domain by the following relation [3]:

$$I(k) \propto \sum_{n=1}^{N} \sqrt{R_n} \cos 2k z_n \tag{1}$$

Where $I(k)$ is the intensity profile as a function of the wavenumber k, z_n is the depth of the nth scattering element, and R_n is the reflectivity of the nth scattering element. This shows that depth information is encoded in the signal by periodic ripples in k-space, with deeper scatterers resulting in lower-periodicity ripples. Applying an inverse Fourier transform to this signal produces a depth-reflectivity profile at a specific lateral point on the retina, called an A-scan. The combination of A-scans along a single lateral direction is referred to as the B-scan, and the combination of B-scans along the other lateral direction is referred to as the tomogram. The axial resolution δz of the A-scan, that is, the ability of the system to distinguish separate point reflectors along z, is defined by the coherence length l_c of the source:

$$\delta z = l_c = \frac{2\ln 2}{\pi} \cdot \frac{\lambda_0^2}{\Delta\lambda_{FWHM}} \tag{2}$$

Specification	Condition	Source
Rod outer segment imaging resolution	$\sim 1\mu m$	
Standard clinical OCT lateral resolution	15-20 μm	[14]
ORG line scan range	$\sim$560 μm	Zhang et al. [19]
Clinical OCT line scan range	12 mm	[14]

TABLE I: Performance Target Outline

Where λ_0 is the central wavelength of the source and λ_{FWHM} is the wavelength range of the source. The lateral resolution of the system is defined by the diffraction-limited intensity FWHM of the beam at the sample, which is related to the gaussian beam waist w_0 by:

$$\delta x = \sqrt{2\ln 2} w_0 = \sqrt{2\ln 2} \frac{\lambda_0}{\pi \mathrm{NA}} \tag{3}$$

Where NA is the numerical aperture of the eye. Considering that a more narrowly-focused Gaussian beam has a greater angle of divergence, improving the lateral resolution decreases the depth of focus of the system:

$$\mathrm{DOF} = \frac{2\pi n}{\lambda_0} w_0^2 = \frac{n\lambda_0}{2\pi \mathrm{NA}^2} \tag{4}$$

Where n is the refractive index of the sample medium. The speed of this technique can be improved by employing a line-scan, where the beam profile at the retina is shaped to be a line field, then mapped back to the second axis of the sensor. This allows for simultaneous collection of A scans to produce a full B-scan in a single frame. A useful property of SD-OCT is that phase information is already encoded within the extracted signal. This allows for the detection of nanoscale deformations in the point scatterers, far below the limit of the axial resolution. Consider, when the nth point scatterer moves axially by some distance Δz, it will induce a phase shift $\varphi \propto k\Delta z$ in the intensity-wavenumber profile of the nth element:

$$I_n(k) \propto \sqrt{R_n} \cos(2kz_n + \varphi) \tag{5}$$

By following this phase shift in k-space over a period of time, it is possible to extract Δz as a function of time, thus allowing for temporally resolved detection of rod deformations.

III. Design & Methods

A. Apparatus

The elements of this system are based on commonly available optical and electronic components. In accordance with Zhuo et al. [21], the optical spectrum is based on the FIR-9 supercontinuum laser from NKT Photonics with the spectrum shaped by a Semock FF01-776/LP-25 long pass filter and a Thorlabs FESH0900 short pass filter to produce a wavelength distribution with $\Delta\lambda_{FWHM}$ = 120 nm centered at λ_0 = 840 nm. This is a typical wavelength range for OCT imaging, as near-IR frequencies allow for deeper tissue penetration than visible light. From Eq. 2, this gives a minimum axial resolution of 2.59 μm. To minimize chromatic aberration in the system, the beam is relayed using achromatic lenses based on Thorlabs AC-254-f-B achromatic doublets (where f is the focal length), which are rated for performance in the 650-1050 nm wavelength range. The line field is shaped using Thorlabs LJ1821L1-B (f = 50 mm) and LJ1054L1-B (f = 75 mm) 650-1050 nm AR coated plano-convex cylindrical lenses. The spectrometer is based on the Wasatch Photonics WP-600/900-25.4 visible volume phase holographic transmission grating, which is designed for near-IR OCT. It has a grating frequency of 600 l/mm, and an optimal angle of incidence of 15.7° at 900 nm. A fairly low grating frequency is selected initially in order to manage aberrations that may be caused by steep dispersion angles. The spectrometer detector plane is based on a GSENSE2020BSI CMOS image sensor, which has a 13.312×13.312 mm photosensitive area, a pixel size of 6.5×6.5 μm over 2048×2048 active pixels. This sensor is chosen due to its relatively high Quantum Efficiency of ∼ 50% at the wavelength spectrum of interest, and its pixel pitch that is smaller than the aberrated beam waists seen in

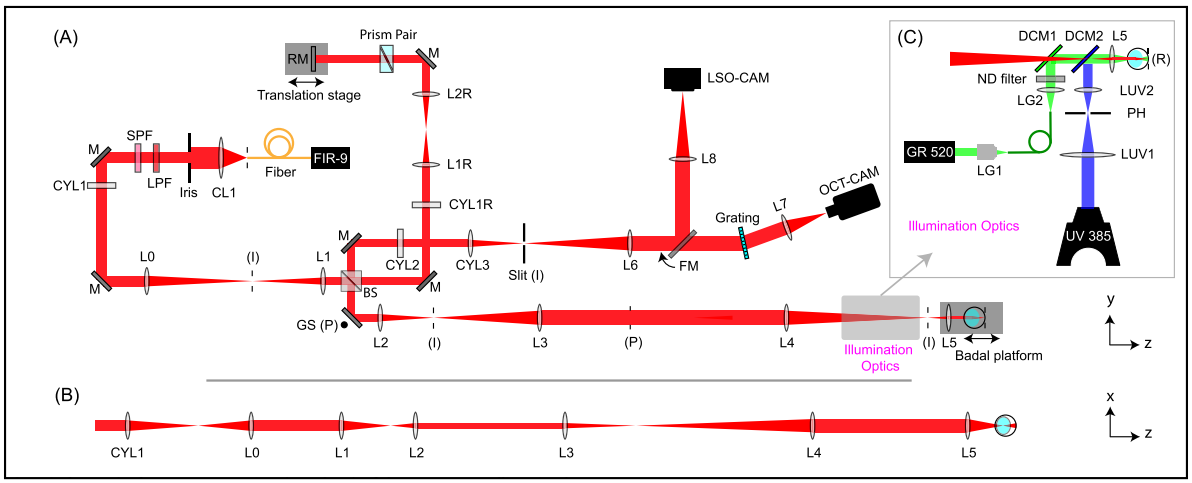

Fig. 3: Optical setup used for OCT imaging and retinal stimulation in rat eye. Excerpted from Fig. 7(a–c) of Zhuo et al. [21].

later sections.

B. Eye Model

The model of the eye used in this project is based on that developed by Navarro et al. [13], with geometry shown in Table II. In this model, the refractive indices at 840 nm are as follows: $n_{CORNEA} = 1.376$, $n_{AQUEOUS} = 1.336$, $n_{LENS} = 1.420$, and $n_{VITREOUS} = 1.336$.

TABLE II: Navarro eye geometric parameters

Surface	Radius (mm)	Thickness (mm)	Asphericity
Cornea (Anterior)	7.72	0.55	-0.26
Cornea (Posterior)	6.50		0.00
Aqueous		3.05	
Lens (Anterior)	10.20	4.00	-3.13
Lens (Posterior)	-6.00		-1.00
Vitreous		16.40	
Retina	-12.00		

The beam incident on the cornea must be manipulated such that a line field is formed on the retina. This is achieved by focusing 1 axis (say, the y-axis) of the beam at the entrance pupil of the eye, such that the beam disperses angularly within the eye and forms the long axis of the line. The x-axis of the beam must be collimated such that the beam is focused on the retina, forming the short axis of the line. Ideally, to achieve optimal imaging resolution, the width of the short-axis of the line must be minimized. This is achieved by maximally saturating the pupil with light along the x-axis in order to increase the numerical aperture, as per Eq. 3. The dilated pupil diameter of the human eye is roughly 6 mm. The NA of the eye may be estimated by considering the eye to be an $f \approx 17$ mm lens in air. At a 3 mm object height, the half angle formed by the focused ray and the z-axis is roughly 10°. This gives an estimate of the numerical aperture: NA $= n\sin\theta = 0.174$. Using Eq. 3, this suggests that the diffraction-limited lateral resolution along the x-axis is $\delta x = 1.809$ μm. The lateral resolution along the y-axis can be predicted by considering the maximum between the diffraction-limited spot size along the y-axis, and the Nyquist limited sampling resolution determined by considering the number of pixels the retinal line is being mapped over. A target 3 mm line field on the retina is chosen, which gives a Nyquist-limited y-resolution of $\delta y = 2 \times 3mm/2048px = 2.930$ μm. This is fairly short in comparison to diagnostic medical line scanning OCT systems, though, for the stated purpose of cellular imaging, a shorter line is desirable. The length of the line field on the retina may be estimated by considering that the angular spread of the beam will be mostly unchanged if it is focused at the entrance pupil of the eye. If we desire a 3 mm line field on the retina, using the $f \approx 17$ mm lens model, we require a half-angular spread of roughly 5° in air. This angular spread can be achieved by any lens ahead of the eye by focusing a variable collimated beam diameter. For an $f = 50$ mm lens, the required 5° half-angle can be obtained with an incident collimated beam radius of ∼4.4 mm, as shown in Fig. 4. The diffraction-limited y resolution can be determined by using this angular spread to compute the y-axis numerical aperture and substituting in to Eq. 3. This gives $\delta y = 3.6$ μm, this is greater than the Nyquist limited resolution, thus the y-resolution should be diffraction limited in this configuration.

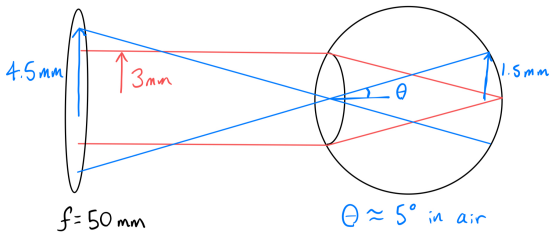

Fig. 4: Simple $f = 17$ mm eye model with $f = 50$ mm focusing lens.

4.

C. Relay Optics

As stated in the previous section, the required beam ahead of the eye is $w = 3$ mm collimated along the x-axis, and focused with a half-angular spread of 5° along the y-axis. An initial beam waist of $w_0 = 4.5$ μm is selected based on a typical mode field diameter of a beam exiting a single-mode fibre. This must be expanded to 3 mm and collimated, as required to fill the majority of a dilated human pupil. Using the equation for Gaussian beam width $w(z)$ and solving for a position z such that $w(z) =$ 3 mm:

$$w(z) = w_0\sqrt{1 + (\frac{\lambda_0}{\pi w_0^2}z)^2} \tag{6}$$

This equation holds for $z = 50.49$ mm, thus, an $f = 50$ mm lens placed 50 mm after the fiber will produce a 3 mm radius collimated beam. As previously stated, the beam radius along the y-axis must be expanded to 4.4 mm. This is achieved by placing 2 cylindrical lenses with $f_1 = 50$ mm and $f_2 = 75$ mm in an afocal telescope configuration, shown in Fig. 5. The output beam waist is proportional

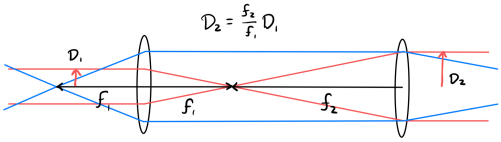

Fig. 5: Afocal telescope diagram.

to the ratio of the lens foci: $w_2 = \frac{f_2}{f_1} w_1$. Thus the output beam waist along this axis is 4.5 mm. The elliptical beam is propagated through a power beam splitter, which separates the sample and reference arms. To produce the line field, another f = 50 mm cylindrical is placed oriented along the x-axis roughly 100 mm ahead of the 50 mm spherical lens focused at the eye. In this configuration, the y-component with w = 4.5 mm passes through the cylindrical lens and is focused at the entrance pupil by the final spherical lens, creating the required angular spread for the line-field, and the x-component forms another 1:1 afocal telescope with the final lens, resulting in a collimated w = 3 mm beam at the entrance pupil, as seen in Fig. 7. The scanning mirror must be placed at a location conjugate to the pupil plane. One such point exists at the front focus of the final cylindrical lens. The beam scatters from the retina and back-propagates through the final 2 lenses before being recombined with the reference arm and propagating to the sensor. A series of lenses consisting of an f = 50 mm cylindrical lens oriented along the y-axis, an f = 75 mm achromat, and an f = 100 mm achromat are placed in afocal telescope configurations as before, expanding the y-axis of the beam to 6.6 mm, then the x-axis of the beam to 4 mm before arriving at the spectrometer. The y-axis is expanded to this width in order to maximally saturate the 13.312 mm height of the sensor, and the x-axis radius is increased to slightly improve the minimum width of the spectral lines when focused at the sensor.

D. Spectrometer

The spectrometer is constructed using the 600 l/mm diffraction grating, the CMOS sensor, and a pair of f = 100 mm achromatic doublet lenses. The first lens in the spectrometer is the final lens mentioned in the previous section. This collimates the beam along the x-axis and focuses the beam along the y-axis. The diffraction grating is placed at the focal point of this lens with its diffraction axis oriented in the x-direction and tilted at its stated AOI of $\alpha = 15.7°$, rotated about the y-axis. The diffraction angle β is given by:

$$d(\sin\alpha - \sin\beta) = m\lambda \tag{7}$$

Where d is the line spacing of the grating. For a 600 l/mm grating, d = 1667 nm. Solving for β gives

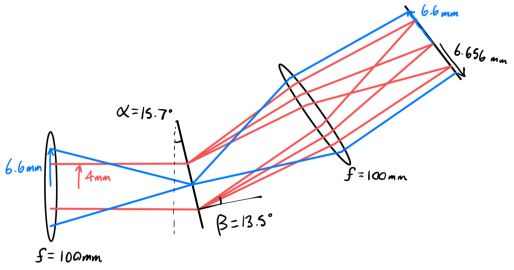

Fig. 6: Spectrometer design.

13.5°, so the second lens is placed at this angle, 100 mm after the grating. The sensor is placed 1 focal length behind the final lens, such that the spectrally-separated field components along the x-axis are in focus. Considering that this forms another 1:1 afocal telescope with the previous lens, the output beam is 6.6 mm and collimated along the y-axis, which is roughly the half-width of the sensor, as desired. The spectrometer configuration is shown in Fig. 6. The output of the spectrometer should contain the spectrally-encoded depth information along the x-axis, and lateral retinal points along the y-axis. Per the Nyquist sampling theorem, the FWHM width spanned by a single spectral line on the detector should be greater than 2x the pixel pitch of the detector in order to accurately resolve the ripples encoded in the frequency spectrum. The expected FWHM spot size for a lens focusing a collimated beam is:

$$\text{FWHM} = \sqrt{2\ln 2}\frac{\lambda f}{\pi w_0} \tag{8}$$

For the 4.4 mm beam in the x-axis, this results in a diffraction limited FWHM of 7.15 μm, which is sub optimal for a pixel pitch of 6.5 μm. However, the presence of aberrations in the system will likely result in a spectral line width that more closely satisfies this condition.

Spectrometer design calculations and close-up figure. Detector sampling requirements.

E. Other Components

There are a number of components that were not explicitly included in CODE V simulations, as they are less relevant to the performance of the free space optical system, however, they are necessary for obtaining experimental results in a real system. These include a green laser source and a dichroic mirror which is inserted into the optical path to the retina, allowing for the administration of green flashes that are required to stimulate rapid contraction in the retinal rod outer segments [21]. The UV flash used by Zhuo et al. to reverse this contraction was not included in the system, as the human eye, unlike that of rodents, absorbs UV light.

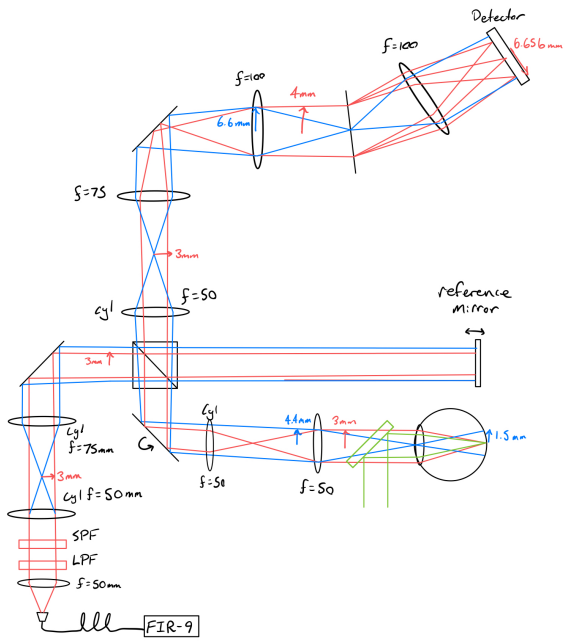

Fig. 7: Full system sketch.

The reference arm is also excluded from simulations, as its theoretical design is quite simple, only requiring that the OPL is within 1 coherence length of the sample arm. The coherence length is quite small, being equal to the axial resolution of 2.59 μm. This range can be located by placing the reference mirror on a translation stage which may be tuned until the OPL condition is met. Zhuo et al. also include a prism pair in the reference arm to balance dispersion mismatch between the sample and reference arms [21].

IV. Simulation and Results

A. Source to Eye

The lenses were placed along the path from the source to the eye, as shown in Fig. 7. The exact placement of the lenses was determined sequentially by varying the lens spacing and ensuring that the output beam was collimated along the desired axis by observing the beam waist values at large distances using the Gaussian beam trace tool. The eye was placed at the end of the system using the Navarro eye model from Tab. II. The V-number is set to 99.9999 to simulate a low-dispersion eye. The distance from the posterior lens to the retina was varied slightly to find the minimum beam waist.

The ideal retinal beam waist in this system was determined to be 1.5 μm along the x-axis and 1.5255 mm along the y-axis using the output of the Gaussian beam trace tool, as expected. This corresponds to an x-resolution of $\delta x = 1.766$ μm. Beam Synthesis Propagation was then used to determine the realistic aberrated line width on the retina. A 4.5 × 4.5 μm input beam consisting of 780 nm, 840 nm, and

Surface #	Surface Name	Surface Type	Y Radius	X Radius	Thickness	Glass	Refract Mode	Y Semi-Apert	Non-Centered Data
Object	Fibre Output	Sphere	Infinity	Infinity	44.4800		Refract		
Stop	Entrance Pupil	Sphere	Infinity	Infinity	5.0000		Refract	5.0000	
2	AC254-050-B no.1	Sphere	33.5500	33.5500	7.5000	NLAK22_SCHOTT	Refract	12.7000	
3		Sphere	-27.0500	-27.0500	1.8000	NSF6HT_SCHOTT	Refract	12.7000	
4		Sphere	-125.6000	-125.6000	2.0000		Refract	12.7000	
5	Scanning Mirror	Sphere	Infinity	Infinity	0.0000		Refract	10.0000	Decenter & Bend
6		Sphere	Infinity	Infinity	49.5000		Refract	10.0000	
7	LJ1821L1-B no.2	Y Toroid	Infinity	25.8400	4.0100	NBK7_SCHOTT	Refract	10.0000	
8		Y Toroid	Infinity	Infinity	96.5000		Refract	10.0000	
9	AC254-050-B no.2	Sphere	33.5500	33.5500	7.5000	NLAK22_SCHOTT	Refract	12.7000	
10		Sphere	-27.0500	-27.0500	1.8000	NSF6HT_SCHOTT	Refract	12.7000	
11		Sphere	-125.6000	-125.6000	39.9300		Refract	12.7000	
12	Anterior Cornea	Asphere	7.7200	7.7200	0.5500	376000.999999	Refract	12.7000	
13	Posterior Cornea	Asphere	6.5000	6.5000	3.0500	336000.999999	Refract	12.7000	
14	Anterior Lens	Asphere	10.2000	10.2000	4.0000	420000.999999	Refract	12.7000	
15	Posterior Lens	Asphere	-6.0000	-6.0000	16.7430	336000.999999	Refract	12.7000	
Image	Retina	Sphere	-12.0000	-12.0000	0.0000	336000.999999	Refract	12.7000	
End Of Data									

Fig. 8: Source to eye path LDM.

Fig. 9: Source to eye Gaussian beam trace y-z view.

Fig. 10: Source to eye Gaussian beam trace x-z view.

900 nm wavelengths was propagated through the system with the pre-analysis recommended settings. The BSP wavefront aberration warning messages were monitored, and resampling was done at select surfaces when required. The resulting retinal line is shown in Fig. 11. The irradiated line length is

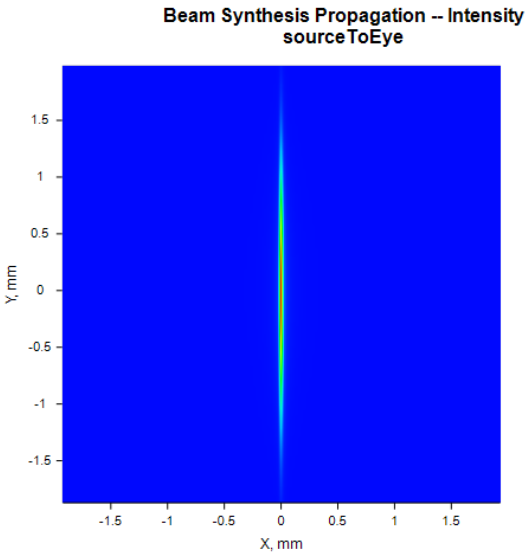

Fig. 11: BSP intensity plot at the retinal surface.

roughly in line with the expected value of 3 mm. The lateral resolution corresponding to this line can be found simply by increasing the mesh accuracy

of the BSP output and manually measuring the intensity FWHM of the line from the 2-D intensity plots. This was measured to be roughly $\delta x = 7.0\ \mu m$, a 296% increase compared to the ideal x-resolution computed from the Gaussian beam trace tool. Evidently, the resolving power has been decreased by aberrations present in the system, either from the eye or from the lenses. Similar BSP plots were produced at 900 nm and 780 nm alone, and it was found that the resolution of the 900 nm component was $\delta x = 6.33\ \mu m$, and 8.228 μm for the 780 nm component.

B. Line Scanning

The optimal location for the scanning mirror was determined by applying a tilt at a location between the second and third cylindrical lenses and observing the chief ray as it passes directly through the entrance pupil of the eye. This distance was determined to be roughly 49.5 mm in front of the third cylindrical lens, shown in Fig. 12. Ray diagrams were used here due to strange behaviour in the Gaussian beam trace visual output after the decenters. BSP was performed at a mirror tilt of

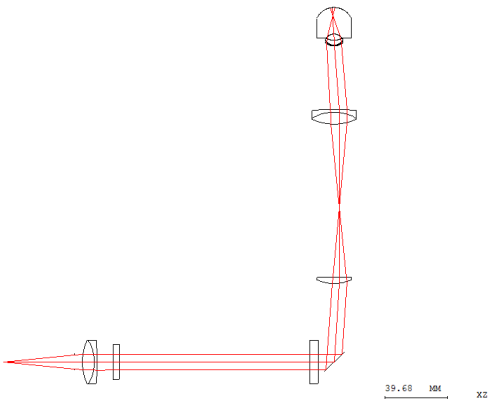

Fig. 12: Folded source to eye path x-z ray trace with 2° mirror tilt.

1°, 2°, and 3°, with results shown in Tab. III. A sample BSP output plot at 2° is shown in Fig. 13. Evidently, the off-axis performance of the scan is quite poor, resulting in a rapid degradation of the lateral resolution away from the centre of the retina.

TABLE III: Measured x-displacement and x-resolution values for variable scanning mirror tilts

Mirror Angle	x-displacement (mm)	$\delta x(\mu m)$
1°	-0.59	10.2
2°	-1.18	25.4
3°	-1.72	95.2

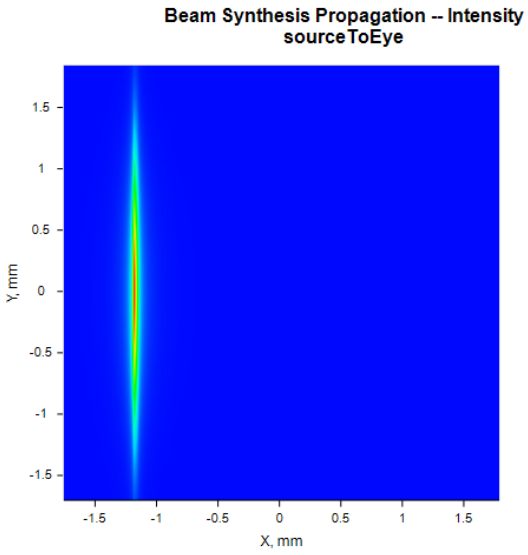

Fig. 13: BSP intensity plot at the retinal surface with 2° mirror tilt.

C. Retinal Beam Waist Verification

Best Fit Gaussian parameters were extracted from `Beam Synthesis Propogation Analysis` to provide another facet of (approximate) verification of the thin-axis retinal waist size and line-length. We ran these measurements on the center, positive and negative extrema of the simulated galvo scan. the results obtained are displayed in IV, with `BSP` settings provided between figures 22 and 27, with only modifications to `X Offset` in the output grid to account for line scan shifts. For these measurements, theoretically, `CODE V` is fitting the reconstructed retinal intensity to an elliptical Gaussian. In that fit:

$$I(x', y') = I_0 \exp\left(-2\frac{x'^2}{w_x^2} - 2\frac{y'^2}{w_y^2}\right) \tag{9}$$

Where `X-RAD` $= w_x$ and `Y-RAD` $= w_y$. These are $\frac{1}{e^2}$ intensity radii, not diameters. Therefore, for our calculations, from the Gaussian intensity profile we have that the $\frac{1}{e^2}$ diameter $= 2w$ and $FWHM = w \times \sqrt{2ln2} = 1.17741w$. For each one of our measurements the calculated values are thus shown in VII. We see again that larger excursions from the center incurr considerable loss in lateral resolution. This is expected as for line-scan ORG, which does not attempt to generate a volume or 3d reconstruction but instead emphasizes axial resolution, the expected scan would only span a couple hundred micrometers, and from that perspective numerically we satisify the lateral resolution critera for scans close to the center line.

D. Cornea to Spectrometer

The lenses and diffraction grating were arranged as shown along the path between the cornea and

detector in Fig 7. The exact placement of the lenses were tuned in a similar manner to the previous sections. The LDM for this system is shown in Fig. 14, and the 3-D ray trace is shown in Fig 15. As before, the Gaussian beam trace is not shown due to non-physical behaviour in the visual output after a decenter.

Surface #	Surface Name	Surface Type	Y Radius	X Radius	Thickness	Glass	Refract Mode	Y Semi-Apert	Non-Centered Data
Object		Sphere	Infinity	Infinity	35.4700		Refract		
Stop		Sphere	Infinity	Infinity	10.0000		Refract	6.0000	
2	AC254-050-B no.2	Sphere	125.6000	125.6000	1.8000	NSF6HT_SCHOTT	Refract	12.7000	
3		Sphere	27.0500	27.0500	7.5000	NLAK22_SCHOTT	Refract	12.7000	
4		Sphere	-33.5500	-33.5500	96.7500		Refract	12.7000	
5	LJ1054L1-B no.1	Y Toroid	Infinity	Infinity	5.1200	NBK7_SCHOTT	Refract	12.7000	
6		Y Toroid	Infinity	-25.8400	50.0000		Refract	12.7000	
7	LJ1054L1-B no.2	Y Toroid	Infinity	Infinity	5.1200	NBK7_SCHOTT	Refract	12.7000	
8		Y Toroid	-25.8400	Infinity	126.2700		Refract	12.7000	
9	AC254-075-B	Sphere	36.9000	36.9000	5.0000	NBAF10_SCHOTT	Refract	12.7000	
10		Sphere	-42.1700	-42.1700	1.6000	NSF6HT_SCHOTT	Refract	12.7000	
11		Sphere	417.8000	417.8000	169.6000		Refract	12.7000	
12	AC254-100-B no.1	Sphere	66.6800	66.6800	4.0000	NLAK22_SCHOTT	Refract	12.7000	
13		Sphere	-53.7000	-53.7000	1.5000	NSF6HT_SCHOTT	Refract	12.7000	
14		Sphere	-259.4100	-259.4100	97.0900		Refract	12.7000	
15	Decenter 1	Sphere	Infinity	Infinity	0.0000		Refract	12.7000	Basic Decenter
16	Diffraction Grating	Sphere	Infinity	Infinity	0.0000		Refract	12.7000	
17	Decenter 2	Sphere	Infinity	Infinity	99.6800		Refract	12.7000	Basic Decenter
18	AC254-100-B no.2	Sphere	66.6800	66.6800	4.0000	NLAK22_SCHOTT	Refract	12.7000	
19		Sphere	-53.7000	-53.7000	1.5000	NSF6HT_SCHOTT	Refract	12.7000	
20		Sphere	-259.4100	-259.4100	97.0950		Refract	12.7000	
Image		Sphere	Infinity	Infinity	0.0000		Refract	6.6560	
End Of Data									

Fig. 14: Cornea to detector path LDM.

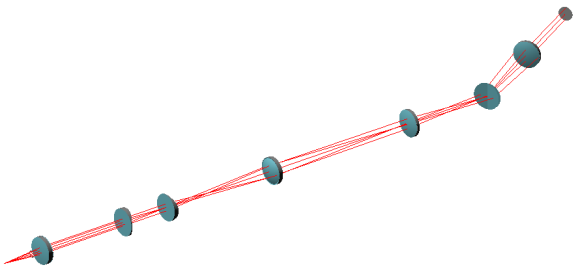

Fig. 15: Cornea to detector path 3-D ray trace view.

The initial Gaussian beam parameters were determined by measuring the x and y axes of the beam at the minimum y-axis beam waist near the entrance pupil of the eye in the previous simulation. These were determined to be 2.9380 mm along the x-axis and 3.0 μm along the y-axis. A BSP was performed at 900 nm, 870 nm, 840 nm, 810 nm, and 780 nm. The resulting intensity plot is shown in Fig. 16, and the spectral line data is shown in Tab. V. The spectral lines appear to occupy a range of 12 mm along the y axis of the detector, and a range of 7.39 mm along the spectral axis.

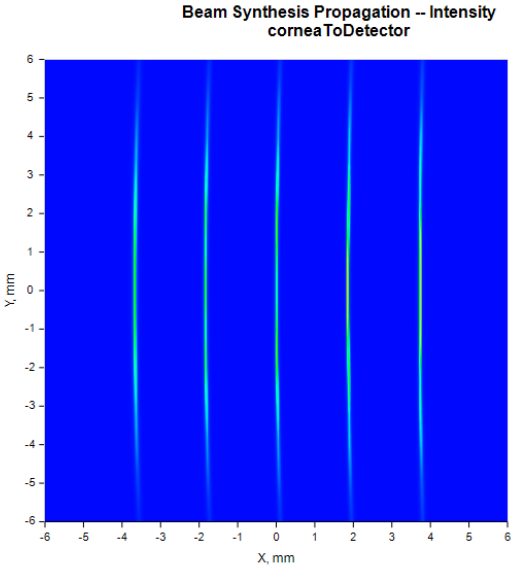

Fig. 16: BSP spectral lines in the detector plane for the cornea to detector path.

TABLE V: Spectral line position and intensity FWHM at the plane of the detector.

Wavelength (nm)	Position (mm)	Line width (μm)
780	-3.68	23.8
810	-1.84	17.8
840	0	17.6
870	1.86	17.6
900	3.71	17.8

β (Surface 16)	wavelength (nm)	X-RAD (mm)	Y-RAD (mm)	X-SHIFT (mm)	RMS ERROR
	900	0.006161	1.422574		0.036165
22.5°	840	0.007140	1.357533	0	0.040351
	780	0.010446	1.299401		0.099823
	900	0.023988	2.189694		2.189694
20.5°	840	0.027236	1.722410	-1.156	0.213187
	780	0.031016	1.506943		0.177078
	900	0.023108	2.118368		0.264580
24.5°	840	0.026570	1.721197	1.156	0.207179
	780	0.030500	1.507868		0.174104

TABLE IV: Best Fit Gaussian Parameters across wavelengths and galvo positions

E. Aberration Correction

To explore methods for correcting geometric aberrations in the eye, a Fringe Zernike Polynomial surface is tested on a collimated beam incident on the Navarro eye model, shown in Fig. 17. A

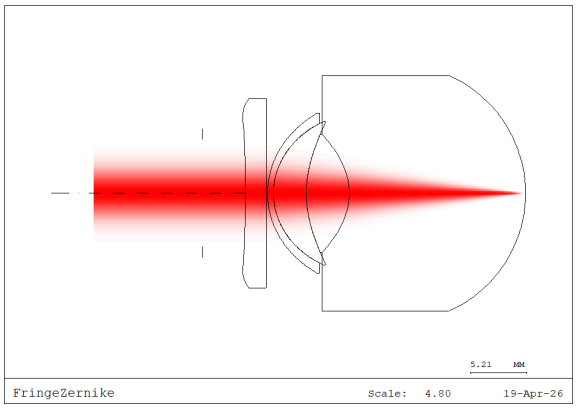

Fig. 17: Gaussian beam trace of Navarro eye with Fringe Zernike Polynomial surface.

piece of BK7 glass was placed in front of the eye, and the surface type was set to Fringe Zernike Polynomial. This surface can be used to introduce aberrations to an optical wave that are opposite to the aberrations introduced by another element in the system, resulting in a cancellation of the target aberration sources. The on-axis geometric aberrations in the eye were considered by varying the angle-independent terms of the Fringe Zernike polynomial, corresponding to piston, defocus, and higher order spherical aberration terms. These terms were tuned for Gaussian beam performance by using the automated design feature and minimizing wavefront error. This resulted in the coefficients: Z_1 = -0.0670, Z_4 = -0.0755, Z_9 = 0.0292, Z_{16} = 0.0494, and Z_{25} = 0.0118. The BSP results for a 3 mm radius collimated Gaussian beam are shown in Figures 15 and 16. Without correction, the retinal FWHM spot size was 5.95 μm. By adding the fringe Zernike polynomial surface, the spot size was reduced down to 2.37 μm, a reduction of -60%, and which is only 58% greater than the minimal spot size of 1.5 μm.

V. Analysis & Discussion

A. Performance Evaluation

There are 2 major thresholds that may be considered when evaluating this system's lateral resolution performance. The first is the typical lateral resolution of 15-20 μm achieved by commercial medical OCT scanners [2]. At this resolution, macro-structures within the retina are distinguishable, making the system sufficient for diagnostic medical imaging. The second threshold is the target resolution required to distinguish the rods and cones

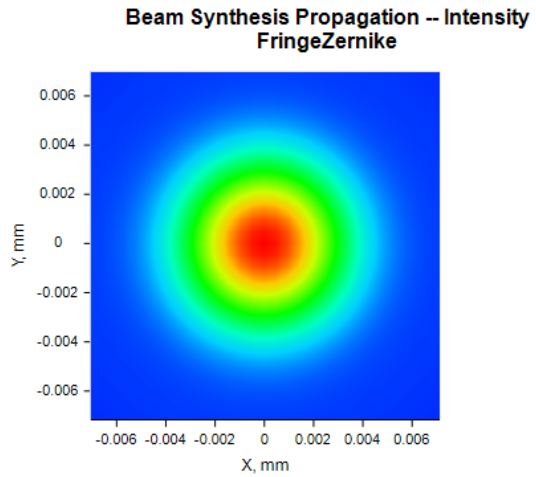

Fig. 18: BSP intensity plot at retinal surface before aberration correction.

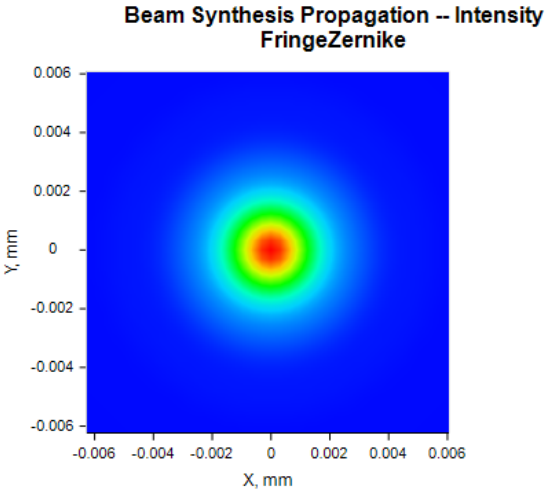

Fig. 19: BSP intensity plot at retinal surface after the addition of a Fringe Zernike surface.

in the eye, which are typically around 2 μm in diameter. Per the rule of Nyquist sampling, the resolution required would be 1 μm or less. This resolution was not obtainable using OCT in the human eye, as even in the ideal case, the diffraction limited resolution could not be reduced below 1.76 μm. Even when considering the maximal obtainable numerical aperture from a fully dilated human eye, NA≈0.23, the lateral resolution is 1.36 μm at minimum. Thus, this is simply a limit of the imaging technique. However, the system performs quite well in comparison to clinical OCT scanners, achieving δx = 7.0 μm, including aberrations, well below the threshold required for macro-structural imaging.

However, when performing the line-scan, the resolution rapidly degrades to a level below the clinical OCT level at roughly ±1 mm from the centre of the retina, as seen in Tab. III. This is

quite narrow compared to clinical OCT scanners, such as the RTVue Fourier-Domain Optical Coherence Tomography System, which can achieve scanning ranges up to 12 mm. This is likely due to inaccuracy in the placement of the scanning lens at a point conjugate to the pupil. It could also be due to the use of a simple cylindrical lens in the scanning mirror-to-eye relay telescope, which could exaggerate chromatic aberrations off-axis.

It was also found in section IV-D that the spectral lines at the detector generally have a width of $\sim$17.7 μm, roughly 2.7$\times$ the 6.5 μm pixel pitch of the detector. This is in the ideal sampling rate range required to correctly distinguish the spectral components, per the Nyquist sampling theorem.
It is also worth noting that exact measurements of the retinal line length were avoided in this project, and were left intentionally vague. As seen in previous detector-plane plots, the intensity of the lines taper off gradually as a function of y, and would only "stop" once the minimum detectable intensity by the sensor is surpassed. Thus, we believe that the effective line length is a function of the detector's required optical SNR, and cannot be accurately measured using easily extractable figures from CODE V.

Overall, the performance of the system is satisfactory for the purpose of retinal imaging and phase sensitive measurements, and may be easily replicated in reality, due to the intentional selection of commonly available optical elements that are compatible with table-top optical mounts.

B. Phase Considerations

One form of aberration that must be considered in a realistic system is the optical path difference error inherent to the optical geometry of the system. Since different points along the y axis do not travel the same OPL, they will arrive out of phase and degrade the received signal [1]. This would need to be corrected in signal processing by subtracting a y-dependent "background" phase term characterized by the variable OPL through the system at different y-axis heights from the received signal. An example of the y-dependent phase shift is shown in Fig. 20

The temporal phase sensitive measurements required to detect the nanoscale deformations in the rods cannot be simulated in code V, and is mainly in the domain of signal processing, rather than optical system design. However, certain measures can be taken in anticipation of phase noise that may degrade phase sensitive measurements. Small phase impairments may be caused by environmental factors such as vibrations and air turbulence. This is mitigated somewhat in the design by ensuring that the sample and reference arms share a common path for as long as possible. In such a configuration, phase noise along the shared path is applied as a global phase term to both the sample and reference arms, which has minimal effect the differential phase sensitive interferometric measurements.

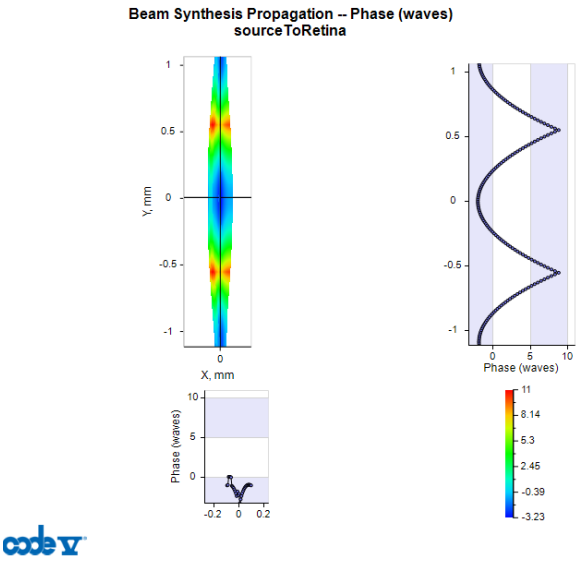

Fig. 20: BSP wrapped phase difference along the y-axis of the retinal line.

C. CODE V Implementation Issues

There were a number of difficulties that were encountered when attempting to add elements of aberration correction and realism to the system. Notably, the Fringe Zernike polynomial surface used in section IV-E is a radial function. This does not work in the main system due to the astigmatic design of the beam. A similar method was attempted by applying an even polynomial surface across the x-axis only, and optimizing the 2nd, 4th, 6th and 8th order coefficients corresponding to the powers of the radial Zernike function that were optimized previously by minimizing wavefront error. The results of these optimizations were highly unstable and did not produce usable results.

There were also issues encountered when attempting to increase the range of the scan while using BSP. BSP requires ray traces to be unobstructed prior to running, this results in the rays being clipped at sharper scan angles, and the BSP being unable to run. This can be reduced by decreasing the diameter of the stop surface, however, the stop surface diameter must remain wide enough to allow the beam passage. As such, scan angles greater than $\sim$3 could not be obtained.

The full back-propagation of the beam returning from the eye to the spectrometer was also not included, as the initial beam parameters required to mimic the beam as it would be if it were reflected from the retina was not obtainable using BSP settings. As such, the spectrogram at the detector is much more idealized than reality, as it does not

include aberrations from the eye. It may be possible to characterize the aberration contributions by the eye at the detector by replacing all cylindrical lenses with equivalent spherical lenses and starting with a point-beam waist, then observing the spectral point spread on the detector, as would be done in point SD-OCT. The FWHM of these points would likely correspond closely to the width of the spectral lines in our system, allowing the eye aberrations to be measured and mitigated.

D. Assumptions

In addition to those mentioned above, a few simplifying assumptions were made in order to lower the complexity of the system. These are mainly centred around the model of the eye. The first of which was assuming a fairly non-dispersive eye, which was modelled by setting the V-number at every eye surface to 99.9999. Though not exact, this is a fairly safe assumption to make, as the refractive indices of the layers of the eye vary very little in the near-IR wavelength range.

Another simplification was made by varying the distance from the lens to the retina by fractions of a millimetre in order to find the optimal retinal focus position. This is evidently not possible in a real experiment, however, a similar effect may be achieved by slightly varying the location of the final lens before the eye, so that the x-axis of the beam converges or diverges slightly before being focused by the eye, leading to a small axial translation of the beam waist.

Additionally, the inclusion of the gradient-refractive index property of lens was neglected by using the Navarro model of the eye, which may have negatively impacted the performance of the system, as the GRIN lens helps to reduce aberrations in the eye and would improve the simulation results, in addition to being more realistic.

The initial mode-field-diameter of the laser was assumed to be 9 μm, however, this is only true for standard SMF-28 at telecom wavelengths. In reality, the MFD is a function of the optical mode confinement in the fibre core, which is a function of wavelength. A more realistic MFD at 840 nm is $\sim$5.0 $\pm$ 0.5 μm, based on the specifications of Thorlabs' SMF-780HP at 850 nm. This would require a shorter focal length collimating lens to obtain the same 3 mm radius beam required by the system.

E. Design Trade-offs & Improvements

Certain trade-offs were considered when designing this system. For the spectrometer, there is a trade-off between aberration resilience and resolving power when selecting the lenses and diffraction grating. It was noted previously that the spectral components only saturated $<$ 8 mm of the detector, out of the total 13.312 mm. This may contribute to increased cross-talk between frequency components and a lower spectral axis resolution. This span may be increased with a higher grating frequency, which increases the angular spread of the diffracted components, and a shorter focal length lens pair, which may be required to adequately capture the divergent rays. This would saturate a greater area on the detector, however, this configuration increases off-axis aberrations due to the steeper ray angles incident on the lenses.

Another component worth investigating was mentioned in the performance evaluation section, where it was stated that the line-scan performance was quite poor, and it was suggested that this could be due to the use of a non-achromatic cylindrical lens in the relay telescope between the scanning mirror and the eye. This performance may be improved by inserting another 1:1 relay telescope consisting of only achromatic doublets in front of the eye, and placing the scanning mirror at the focus of this relay, as shown in Fig. 21. The results of this improved scan are shown in Tab. VI. Evidently, the off-axis resolution has been improved, with the resolution at 1° improving by $\sim$-19%, $\sim$-44% at 2°, and $\sim$-66% at 3°, for roughly equivalent x-displacements along the x-axis. This is still quite a narrow scan range in comparison to medical OCT systems, though this may be improved by using shorter focal length lenses in the relay to enable sharper angles. Furthermore, this configuration doubles the number of lenses present in the sample arm, which could introduce more differential phase noise in a real system, so the sample-reference arm beam splitter would need to be shifted 2 lenses forward in the optical path. It should also be noted that the third to last lens becomes technically redundant in this system, but its removal would reverse the polarity of the system, that is, the x-axis would become the line-axis, and the y-axis would become the scanning axis. As such, all rotationally asymmetric optics downstream of this lens on the path to the sensor would need to be rotated 90 degrees to accommodate.

TABLE VI: Lateral resolution and translation along the retina for the improved scanning mirror to eye relay.

Angle (°)	$\delta x(\mu m)$	$\Delta x(mm)$
0	7.28	0.000
-1	8.23	0.583
-2	14.24	1.158
-3	32.28	1.720

Finally, while it was shown that Fringe Zernike Polynomial surfaces can be used to correct aberrations in the eye and approach the diffraction limited retinal spot size, this is not a realistic implementation of this design principle, as it would

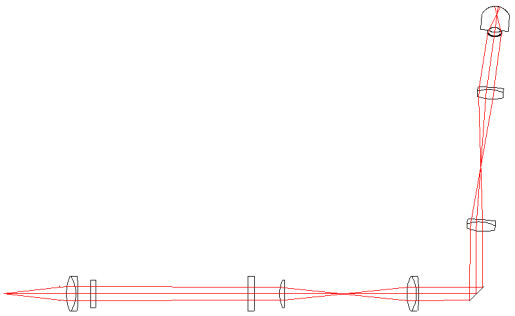

Fig. 21: Ray trace of the source to eye path with additional achromatic relay telescope.

require a uniquely shaped piece of glass for each possible configuration of an eye. In real systems, these principles are implemented through the use of adaptive optics, where a wavefront sensor is used to detect wavefront errors. [6] This information is then relayed to a deformable mirror which shifts to counteract the errors, resulting in a reduction of geometric aberrations. In effect, this is the same as the optimization process used to determine the coefficients of the Zernike polynomial by minimizing wavefront error. [8]

VI. Conclusion

This project presents the design and simulation of a line-scanning spectral-domain optical coherent tomography (SD-OCT) system, with the combined purpose of retinal imaging and detecting nanoscale deformations in the rod outer segments using phase sensitive OCT. The illumination optics are designed to produce a 3 mm line field at the retina, while maximizing numerical aperture at the pupil to attain high lateral resolution imaging, with initial predictions anticipating a diffraction-limited resolution of 1.81 μm. Beam synthesis propagation (BSP) measurements yield a realistic aberrated resolution of 7.00 μm. Line-scanning performance demonstrates measurable lateral displacement with mirror tilts up to 3°, though resolution degrades significantly off-axis, highlighting sensitivity to relay telescope alignment and chromatic effects in cylindrical optics. An alternative relay optic design is proposed and demonstrates greatly improved angular scanning performance, decreasing resolution by -19%, -44%, and -66% at 1°, 2°, and 3° off-centre. The spectrometer design successfully distributes spectral components across ∼7.4 mm of the detector with line widths of ∼17.7 μm, satisfying Nyquist sampling requirements for the 6.5 μm sensor pixel pitch and enabling accurate recovery of spectral domain interference fringes. Further simulations show that introducing Fringe Zernike Polynomial based aberration correction can reduce the lateral resolution by as much as 60%, illustrating the impact of adaptive-optical wavefront correction for approaching diffraction-limited imaging performance. While assumptions such as an idealized eye model and a simplified return path constrain the accuracy of the simulated sensor response, the system is able to achieve resolution well below conventional clinical OCT scanners, though, the requirements for cellular imaging are not obtained and it is revealed to be a fundamental limit of OCT. Overall, the design and results provide a feasibly replicable framework for conducting phase-sensitive retinal deformation measurements in the human eye, and suggest clear pathways for future improvements to the system's performance.

Appendix

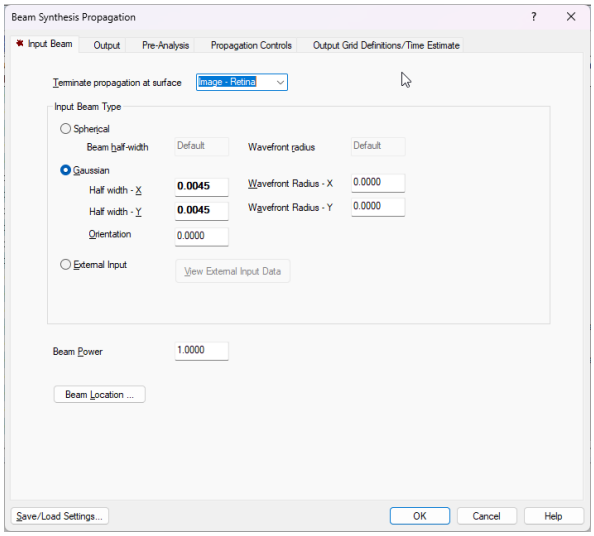

Fig. 22: Example BSP input beam tab

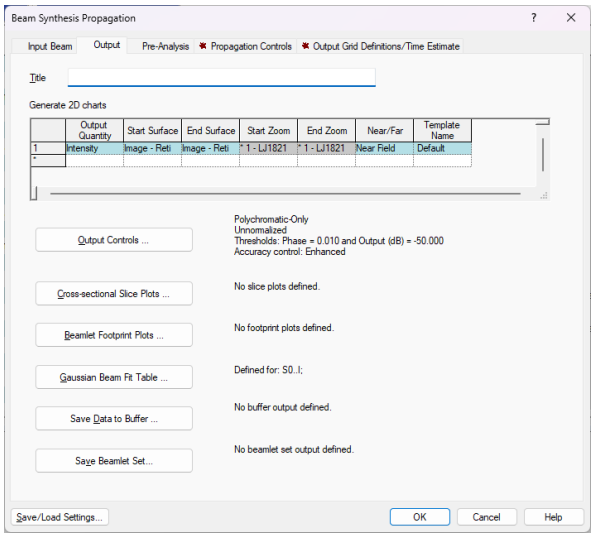

Fig. 23: Example BSP output tab

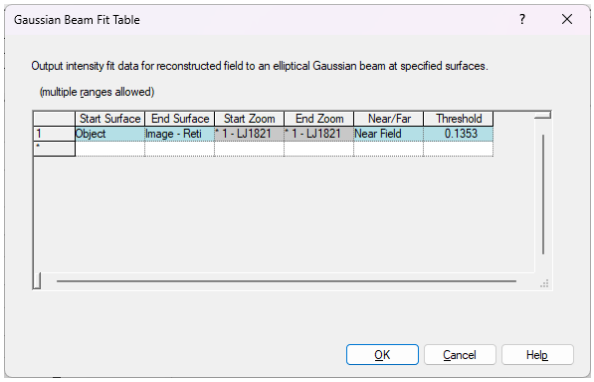

Fig. 24: Example BSP gaussian beam fit table

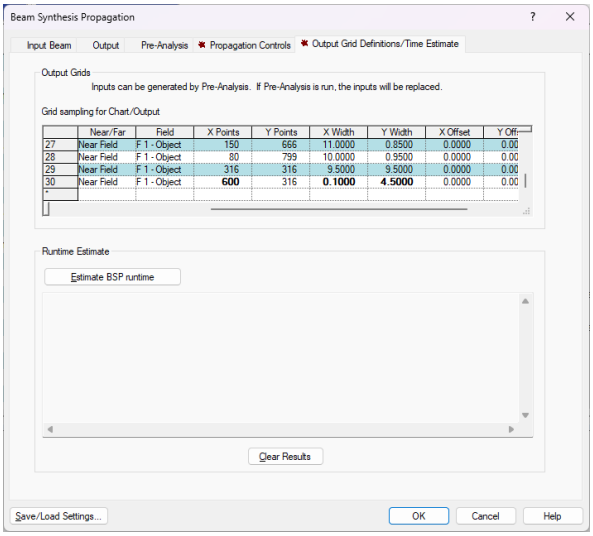

Fig. 25: Example BSP output grid definitions tab, bolded are settings for image surface

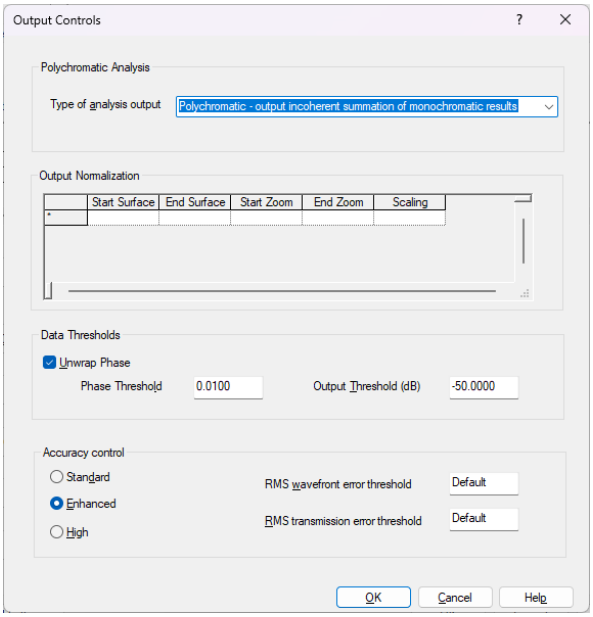

Fig. 26: Example BSP output controls

References

[1] Di Liu et al. “Dispersion correction for optical coherence tomography by the stepped detection algorithm in the fractional Fourier domain”. In: *Opt. Express* 28.5 (Mar. 2020), pp. 5919–5935. DOI: 10.1364/OE.379653. URL: https://opg.optica.org/oe/abstract.cfm?URI=oe-28-5-5919.

[2] RF Spaide et al. “Lateral Resolution of a Commercial Optical Coherence Tomography Instrument.” In: *Transl Vis Sci Technol.* 1.11 (Jan. 2022), p. 28. DOI: doi:10.1167/tvst.11.1.28.

[3] Josef F. Bille, ed. *High Resolution Imaging in Microscopy and Ophthalmology: New Frontiers*

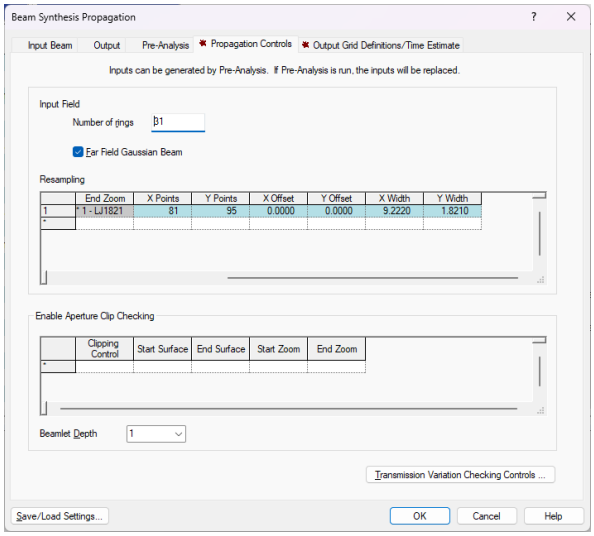

Fig. 27: Example BSP propogation controls

in Biomedical Optics. Cham: Springer International Publishing, 2019. ISBN: 978-3-030-16637-3 978-3-030-16638-0. DOI: 10.1007/978-3-030-16638-0. URL: http://link.springer.com/10.1007/978-3-030-16638-0 (visited on 03/13/2026).

[4] Barry Cense et al. "Volumetric retinal imaging with ultrahigh-resolution spectral-domain optical coherence tomography and adaptive optics using two broadband light sources". In: *Optics express* 17.5 (Mar. 2, 2009), pp. 4095–4111. ISSN: 1094-4087. DOI: 10.1364/oe.17.004095. URL: https://pmc.ncbi.nlm.nih.gov/articles/PMC2715891/ (visited on 04/20/2026).

[5] Khushmeet K. Dhaliwal et al. "Visual stimulus-evoked transient blood flow and blood vessel diameter changes in the healthy human retina measured with a combined OCT+ERG system". In: *Biomedical Optics*

TABLE VII: Calculated $1/e^2$ and FWHM Beam Diameters for Varying Surface Angles and Wavelengths

β	λ (nm)	$1/e^2$ X-DIAM (μm)	$1/e^2$ Y-DIAM (mm)	X-FWHM (μm)	Y-FWHM (mm)
	900	12.322	2.845148	7.254	1.674953
22.5°	840	14.280	2.715066	8.407	1.598373
	780	20.892	2.598802	12.299	1.529928
	900	47.976	4.379388	28.244	2.578168
20.5°	840	54.472	3.444820	32.068	2.027983
	780	62.032	3.013886	36.519	1.774290
	900	46.216	4.236736	27.208	2.494188
24.5°	840	53.140	3.442394	31.284	2.026555
	780	61.000	3.015736	35.911	1.775379

TABLE VIII: Functional Description of Optical Pathways in Multimodal Retinal Imaging and Stimulus Delivery Systems

Optical path	Function
OCT illumination / sample arm	Delivers the OCT beam to the retina as a line field and scans laterally to form B-scans / volumes.
Reference arm	Provides the reference field for OCT interference and depth-resolved measurement.
OCT detection / spectrometer path	Recombines sample and reference light, disperses the spectrum, and records it on a high-speed camera so depth can be encoded.
Stimulus delivery path	Delivers the visual stimulus used to evoke the optoretinographic response.
Auxiliary retinal imaging / alignment path	Provides en face retinal visualization and/or focus/alignment support outside the main OCT spectrometer path.
Adaptive-optics / wavefront-sensing path	Measures ocular aberrations and enables correction for higher-resolution retinal imaging.

Express 16.10 (Oct. 1, 2025), pp. 3958–3976. ISSN: 2156-7085. DOI: 10.1364/BOE.567057.

[6] H. Hofer et al. "Improvement in retinal image quality with dynamic correction of the eye's aberrations". In: *Optics Express* 8.11 (May 21, 2001), pp. 631–643. ISSN: 1094-4087. DOI: 10.1364/OE.8.000631. URL: https://opg.optica.org/oe/abstract.cfm?uri=oe-8-11-631 (visited on 04/20/2026).

[7] K Holopigian et al. "Evidence for photoreceptor changes in patients with diabetic retinopathy." In: *Investigative Ophthalmology & Visual Science* 38.11 (Oct. 1, 1997), pp. 2355–2365. ISSN: 1552-5783. (Visited on 04/20/2026).

[8] Wenhan Jiang and Huagui Li. "Hartmann-Shack wavefront sensing and wavefront control algorithm". In: The Hague '90, 12-16 April. Ed. by Joachim J. Schulte-in-den-Baeumen and Robert K. Tyson. The Hague, Netherlands, Aug. 1, 1990, pp. 82–93. DOI: 10.1117/12.20396. URL: http://proceedings.spiedigitallibrary.org/proceeding.aspx?articleid=941364 (visited on 04/20/2026).

[9] Ravi S. Jonnal. "Toward a clinical optoretinogram: a review of noninvasive, optical tests of retinal neural function". In: *Annals of Translational Medicine* 9.15 (Aug. 2021), p. 1270. ISSN: 2305-5839. DOI: 10.21037/atm-20-6440. URL: https://pmc.ncbi.nlm.nih.gov/articles/PMC8421939/ (visited on 04/21/2026).

[10] Ravi S. Jonnal et al. "Phase-sensitive imaging of the outer retina using optical coherence tomography and adaptive optics". In: *Biomedical Optics Express* 3.1 (Jan. 1, 2012), pp. 104–124. ISSN: 2156-7085. DOI: 10.1364/BOE.3.000104. URL: https://opg.optica.org/boe/abstract.cfm?uri=boe-3-1-104 (visited on 04/20/2026).

[11] Keysight Technologies. *CODE V Optical Design Software*. 2026. URL: https://www.keysight.com/ca/en/products/software/optical-solutions-software/optical-design-solutions/codev.html (visited on 04/20/2026).

[12] Jeremy Nathans. "The Evolution and Physiology of Human Color Vision: Insights from Molecular Genetic Studies of Visual Pigments". In: *Neuron* 24.2 (Oct. 1, 1999), pp. 299–312. ISSN: 0896-6273. DOI: 10.1016/S0896-6273(00)80845-4. URL: https://doi.org/10.1016/S0896-6273(00)80845-4 (visited on 04/20/2026).

[13] R. Navarro, J. Santamaría, and J. Bescós. "Accommodation-dependent model of the human eye with aspherics". In: *J. Opt. Soc. Am. A* 2.8 (Aug. 1985), pp. 1273–1280. DOI: 10.1364/JOSAA.2.001273. URL: https://opg.optica.org/josaa/abstract.cfm?URI=josaa-2-8-1273.

[14] Inc. Optovue. *RTVue Fourier-Domain Optical Coherence Tomography System*. https://www.orangevilleoptometrists.ca/wp-content/uploads/2017/07/RTVue-Optical-Coherence-Tomography-Brochure.pdf. Accessed: 2026-04-20. 2006.

[15] Vimal Prabhu Pandiyan et al. "High-speed adaptive optics line-scan OCT for cellular-resolution optoretinography". In: *Biomedical Optics Express* 11.9 (Sept. 1, 2020), pp. 5274–5296. ISSN: 2156-7085. DOI: 10.1364/BOE.399034. URL: https://opg.optica.org/boe/abstract.cfm?uri=boe-11-9-5274 (visited on 04/20/2026).

[16] Vimal Prabhu Pandiyan et al. "The optoretinogram reveals the primary steps of phototransduction in the living human eye". In: *Science Advances* 6.37 (Sept. 9, 2020), eabc1124. DOI: 10.1126/sciadv.abc1124. URL: https://www.science.org/doi/full/10.1126/sciadv.abc1124 (visited on 04/20/2026).

[17] Dale Purves, ed. *Neuroscience*. 2nd ed. Sunderland, Mass: Sinauer Associates, 2001. 1 p. ISBN: 978-0-87893-742-4.

[18] *Shaping Up What You See: Understanding Rod & Cone Photoreceptors*. Cleveland Clinic. URL: https://my.clevelandclinic.org/health/body/photoreceptors-rods-and-cones (visited on 04/20/2026).

[19] Yan Zhang et al. "Adaptive optics parallel spectral domain optical coherence tomography for imaging the living retina". In: *Optics Express* 13.12 (June 13, 2005), pp. 4792–4811. ISSN: 1094-4087. DOI: 10.1364/OPEX.13.004792. URL: https://opg.optica.org/oe/abstract.cfm?uri=oe-13-12-4792 (visited on 04/21/2026).

[20] Yan Zhang et al. "High-speed volumetric imaging of cone photoreceptors with adaptive optics spectral-domain optical coherence tomography". In: *Optics express* 14.10 (May 2006), pp. 4380–4394. ISSN: 1094-4087. DOI: 10.1364/OE.14.004380. URL: https://pmc.ncbi.nlm.nih.gov/articles/PMC2605071/ (visited on 04/20/2026).

[21] Yueming Zhuo et al. "Interferometric imaging of the reversible rhodopsin dynamics in the living rat eye". In: *Nature Communications* 16.1 (Nov. 28, 2025), p. 10730. ISSN: 2041-1723. DOI: 10.1038/s41467-025-65759-z. URL: https://www.nature.com/articles/s41467-025-65759-z (visited on 03/10/2026).